Blade Displacement Measurements of a Rotor in Forward Flight in the Langley 14- by 22-Foot Wind Tunnel

Edward T. Schairer,[1] James T. Heineck,[2] and Hannah Spooner.[3]
NASA Ames Research Center, Moffett Field, CA, 94035, USA

Austin D. Overmeyer[4]
US Army CCDC Aviation & Missile Center, NASA Langley Research Center, Hampton, VA, 23681, USA

Stereo photogrammetry was used to measure the elastic bending and twist of a three-bladed rotor in forward flight in the NASA Langley 14- by 22-Ft Subsonic Wind Tunnel. The rotor was imaged from below by two cameras mounted at windows of a large turntable in the floor of the test section. At each test condition, the turntable and cameras were rotated and the cameras were triggered to allow measurements over a range of blade azimuth angles. Retro-reflective targets were applied along the leading and trailing edges of the lower surface of each blade. Image blur due to blade motion was minimized by illuminating the targets with high-intensity LED flash lamps mounted next to each camera. The cameras were re-calibrated at each angular position of the turntable using the positions in each image of retro-reflective targets on the ceiling of the test section whose spatial coordinates had been very accurately measured. The blade displacement measurements yielded elastic bending and twist along each blade as functions of blade azimuth, thrust coefficient, and advance ratio, all at a constant rotor shaft angle. In addition, the measurements produced estimates of the rigid-body blade pitch, flap, and lag angles.

I. Nomenclature

r	=	radial distance from rotor shaft, in.
R	=	rotor radius, in.
$\Delta twist$	=	elastic twist, deg.
V_∞	=	Free-stream velocity, ft/sec.
Δz	=	out-of-plane elastic bending, in.
x, y, z	=	distances in the stream-wise, lateral, and vertical directions, in.
C_T	=	Thrust coefficient
α	=	rotor shaft angle of attack, deg.
β	=	rigid-body blade flap angle, positive up, deg.
ζ	=	rigid-body blade lead-lag angle, positive for blade tip leading root, deg.
θ	=	rigid-body blade pitch angle about feathering axis, positive nose up, deg.
μ	=	advance ratio
σ	=	rotor solidity or standard deviation
ψ	=	blade azimuth, 0° over tail, increasing counter-clockwise as seen from above, deg.

II. Introduction

To properly interpret aerodynamic and performance measurements from a wind-tunnel test it is necessary to know the geometry of the test article at test conditions. This is especially important when making comparisons between experimental measurements and numerical simulations. Model deformation measurements (MDM) made by stereo photogrammetry are now widely included in tests of fixed-wing aircraft configurations [1-3]. Stereo photogrammetry has also been used to measure the elastic bending and twist (blade displacement, BD) of helicopter rotor blades in

[1] Aerospace Engineer, Experimental Aero-Physics Branch.
[2] Physical Scientist Engineer, Experimental Aero-Physics Branch, Senior Member of AIAA.
[3] Instrumentation Engineer, Wind Tunnel Division.
[4] Research Scientist, U.S. Army CCDC AvMC.

wind-tunnel tests. The most outstanding example of these measurements were made during tests of the full-scale UH-60A Airloads rotor in the National Full-Scale Aerodynamics Complex (NFAC) 40- by 80- Ft Wind Tunnel [4]. In that test all four rotor blades were imaged by eight digital cameras mounted behind windows in the floor of the test section. This allowed blade displacement measurements over the full 360 degrees of blade azimuth angles at a wide range of forward-flight test conditions.

Elastic deformations are usually measured by marking targets on the test article, measuring the spatial coordinates of the targets at wind-off and wind-on conditions, and comparing the wind-off and wind-on measurements. Before the comparison is made, a subset of targets that are assumed to be rigidly connected is used to account for differences due to rigid-body translations and rotations. For fixed-wing test articles, it is usually not difficult to define a set of well- and widely distributed targets that can safely be assumed to be rigidly connected. In addition, unsteady movement of all targets, including those on flexible parts of the model, is usually minimal. By contrast, a rotor blade is typically flexible from hub to tip so accounting for differences due to rigid-body translations and rotations is problematic. Abrego et al. [4] assumed the inboard targets were rigidly connected and then applied corrections to account for the fact that they really were not. Blade displacement measurements are also more difficult because of the motion of the rotor blades. In forward flight the geometry changes continually and blade displacements are different at each blade azimuth.

Stereo photogrammetry is a good method for measuring the positions of targets on a wind-tunnel model because it can be very accurate and, except for the need for the targets themselves, it is non-intrusive. It does, however, require good views of the test article from at least two directions with significant angular separation, something that is not always possible in wind tunnels with limited optical access (windows). The imaging problem can be especially difficult for rotor measurements because of the motion of the rotor blades relative to the cameras (causing image blur) and because very wide-angle lenses may be required to capture the long, slender blades over the full range of azimuth angles (Abrego et al. had to use fish-eye lenses).

This paper describes blade displacement measurements that were made on a Mach-scale rotor in forward flight in the Langley 14- by 22-Foot Subsonic Wind Tunnel. The test was the second of two tunnel entries the main purposes of which were to measure unsteady boundary-layer transition by thermal imaging with infrared cameras [5-7]. Blade displacement measurements were added to the second test to augment the thermal imaging and also in preparation for blade displacement measurements of the same rotor geometry during hover tests in the NFAC 80- by 120-Ft Wind Tunnel, planned for 2021 (NASA/U.S. Army Benchmark Hover Test, HVAB). In particular, there was interest in demonstrating that elastic twist could be measured to within an uncertainty of 0.1°.

III. Experimental Setup

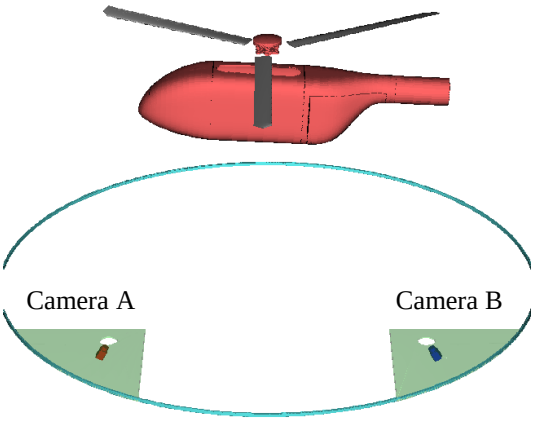

Fig. 1 Schematic showing configuration of the test article, turntable, and cameras.

A. Wind Tunnel

The Langley 14- by 22-Foot Subsonic Wind Tunnel is a closed-circuit, atmospheric wind tunnel. The tunnel can be run with either closed walls or open throat (except for the floor); it was configured with closed walls for the present test. The free-stream velocity (maximum = 348 ft/sec) was set to achieve the desired rotor advance ratio at the rotor RPM (1090).

The floor of the wind tunnel includes a 15.75-ft diameter turntable centered below the model station. Replaceable steel plates in the turntable may be configured for a particular test. For the present test, ports were cut in two panels to accommodate windows for the photogrammetry cameras.

B. Model

The test article was a three-bladed rotor mounted to the General Rotor Model System fitted with a Robin-Mod 7 fuselage. This assembly was supported by a long sting that extended from the tail-boom to a support structure downstream of the turntable (Fig. 1). The rotor plane was seven feet above the floor of the test section.

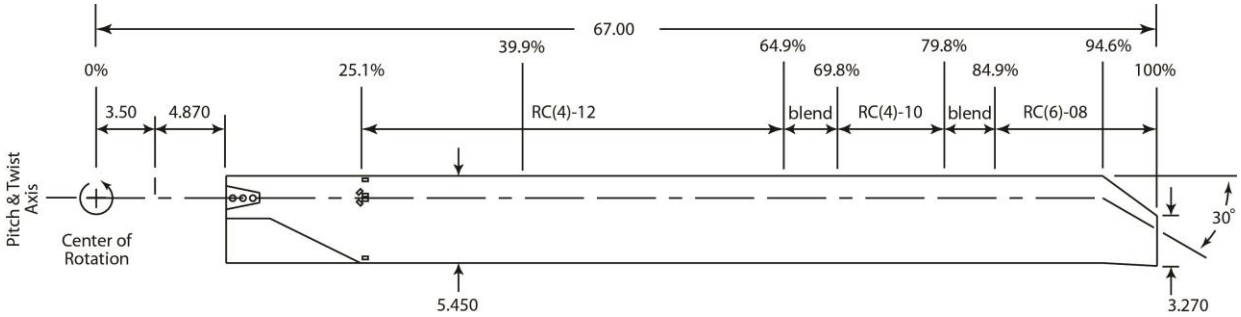

Fig. 2 Planform of PSP rotor blade.

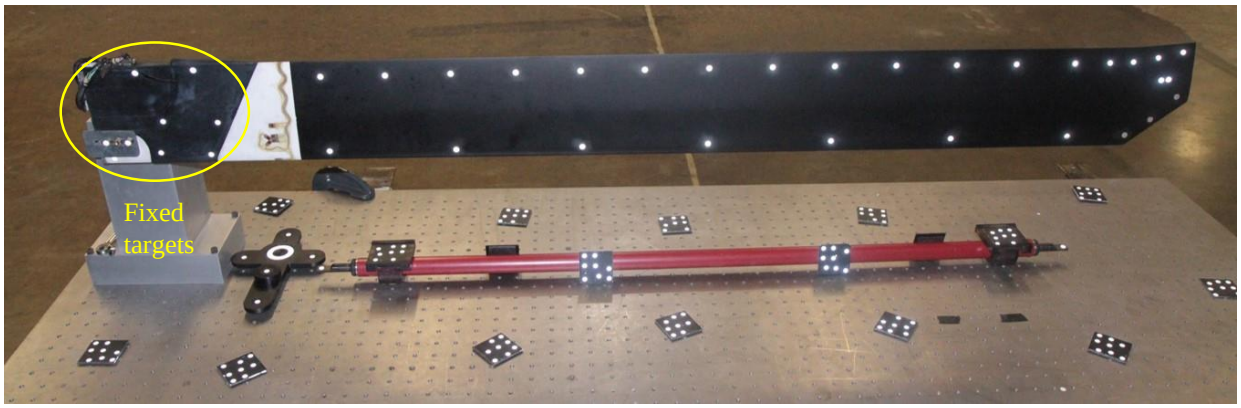

Fig. 3 Rotor blade mounted on optics table for VSTARS measurements of target reference positions.

The radius of the rotor blades (R) was 67 inches. The blades were un-swept except for the outboard 5%, where the leading edge was swept 30° (Fig. 2). The chord of the un-swept portion of the blade was 5.45 inches; the chord at the swept tip was 3.27 inches. The blades use a Government RC-series of airfoils and had a linear twist distribution of -14°. The elastic axis was at the quarter chord. The blades are known as the "Pressure Sensitive Paint (PSP) rotor blades" because they were originally built for use in a PSP validation test in the 14- by 22-Ft Rotor Test Cell. The rotor was fully articulated with the flap and lead-lag hinge co-located 3.5 inches from the rotor shaft.

The blades were painted black to accommodate the IR imagery. Twenty seven adhesive retro-reflective targets (3M 7610, 0.004 inches thick, 0.25-in diameter) were applied along the leading (10) and trailing (17) edges of the lower surface of each blade. In addition, seven targets were distributed inboard of r / R = 0.25 and were used as "fixed" references.

The spatial coordinates of the targets on each un-deformed blade in the blade coordinate system were measured with great accuracy using a commercial photogrammetry system (VSTARS [8], Fig. 3). The blades were supported with the chord line vertical to minimize bending due to gravity. The origin of the blade coordinate system was the center of the rotor shaft. The z axis was coincident with the rotor shaft; the y axis extended along the blade radius and was coincident with the elastic axis (inboard of the swept tip); and the x axis was chordwise, zero at the quarter-chord (inboard of the swept tip). The coordinates measured by VSTARS were used as a wind-off reference against which the coordinates of the same targets at wind-on conditions were compared (after correcting for rigid-body displacements and rotations).

C. Cameras and Lamps

The rotor blades were imaged by two Dalsa Falcon2 12M digital cameras (4096 x 3072 pixels) fitted with 35 mm lenses. The cameras were mounted to structure of the 15.75-ft diameter turntable in the floor of the test section immediately below the test article. To accommodate the cameras, windows had been cut in replaceable steel panels in the upper surface of the turntable (Fig. 1). The distance of both cameras from the center of the turntable was about one rotor radius (R), and the angle between their optical axes was approximately 60°. The cameras were triggered by a once-per-rev signal from the Rotor Azimuth Synchronization Program (RASP [9]) with a delay corresponding to the desired blade and blade azimuth. Images from the cameras were streamed to a digital video recorder and downloaded at the end of each day.

Fig. 4 Camera and lamps installed at one window in turntable.

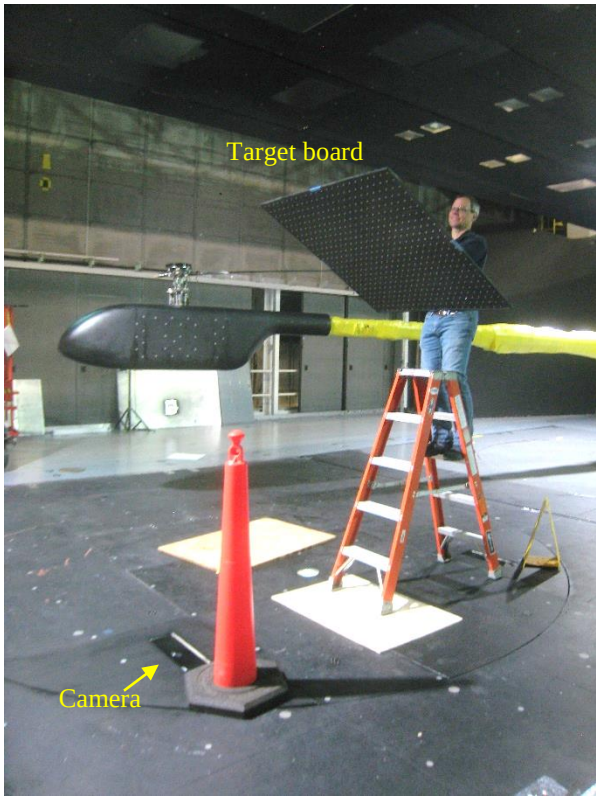

Fig. 5 Imaging target board for internal calibration of camera. Model has been yawed out of the way.

Two high-intensity white-light LED flash-lamps (IDT Constellation 120E) were mounted next to each camera (Fig. 4). Co-locating the lamps with the cameras maximized light return from retro-reflective targets on the rotor blades and test section ceiling. The lamps were triggered by the same once-per-rev signal as the cameras and the flash duration was 10 μs.

D. Camera Calibration

Each camera was calibrated independently using a "pinhole" model. First, with the turntable set for ψ = 270°, both cameras were positioned, pointed, and focused on a static rotor blade propped at approximately ψ = 270° and β= 0°. Then, the rotor blade was moved out of the way and a flat, four- by-four-foot target board was hand-held at the position of the blade (region of interest, ROI). The target board was marked with a 25-by-25 square array of white circular targets on a black background. A sequence of images of the target board was acquired with each camera where the orientation of the board relative to the camera was different in each image, e.g., normal to the optical axis, pitched up/down, yawed left/right, rotated 90°, etc. (Fig. 5). After the targets had been located in each image, and knowing the in-plane spatial coordinates of targets on the board, the internal orientation of each camera (focal length, principal point, skew, lens distortion) was computed using the method of Zhang [10]. The position and point angles (external orientation) of each camera were then computed from the internal orientation and the image- and object-space coordinates of targets on the ceiling of the test section (Fig. 6). The object-space coordinates of these targets in the tunnel coordinate system had been measured with great accuracy using VSTARS. The external orientations of both cameras were re-computed at each angular position of the turntable. The origin of the tunnel coordinate system was at the rotor shaft at α = 0°. Tunnel x and y axes were in the free-stream and cross-stream directions, respectively; the z axis was vertical with zero at the plane of the rotor.

E. Rotor Data System

The rotor shaft pitch and roll angles were measured by on-board Q-flex accelerometers [11], with an uncertainty of 0.004°. The blade root angles were measured relative to the rotor shaft.

Each of the three blades was instrumented with independent pitch, flap, and lag sensors on the blade cuffs. The sensors measured the blade angles directly and there was no cross-coupling of the measurements. The layout of the sensors is shown in Fig. 7. The sensors were custom Hall Effect devices that were calibrated in-situ. The flap and pitch sensors were calibrated using a gravity-based inclinometer on the blade cuff. The rotor shaft angles, measured by the Q-flex, were subtracted from the inclinometer reading for the respective axis to achieve the angles in the rotor shaft coordinates. The lag sensors were calibrated using scribed templates and a pointer on the blade cuff. The uncertainty of each sensor was calculated from the calibration data.

The rotor shaft azimuth was measured with a 1024/revolution optical encoder with a 1/revolution signal at zero degrees azimuth over the tail. The blade angle measurements were acquired at 10 kHz then resampled at 512/revolution resulting in an azimuth resolution of about 0.7°.

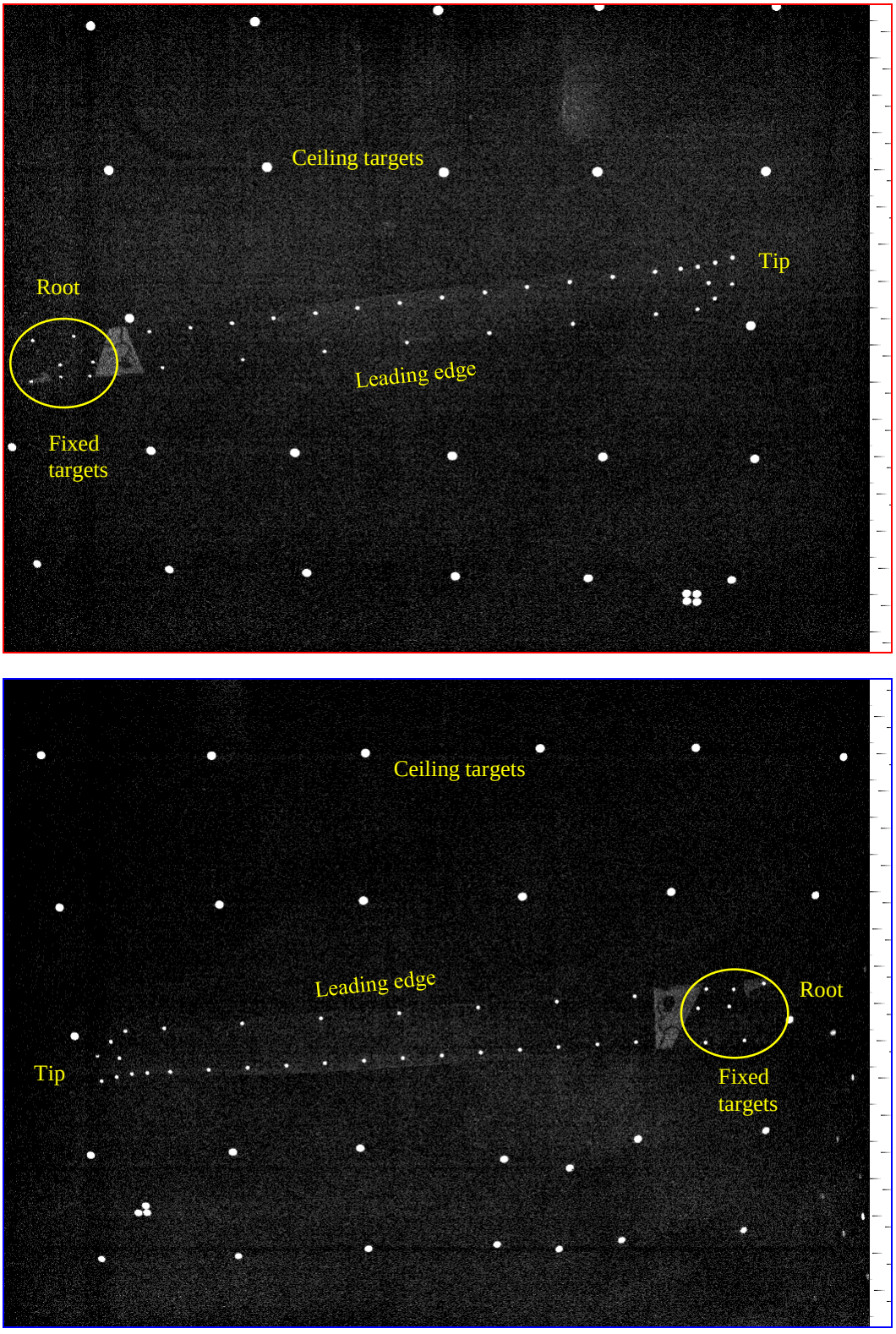

Fig. 6 Typical images from photogrammetry cameras A (top) and B (bottom).

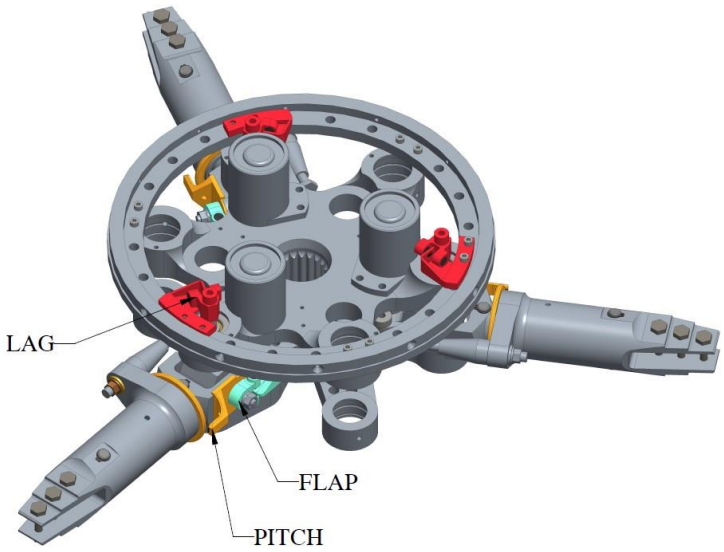

Fig. 7 Rotor hub showing Hall Effect sensors for pitch, flap, and lag.

At each test condition (advance ratio and thrust coefficient), blade displacement images were acquired at a sequence of blade azimuth angles separated by 7.5°. Typically, images were acquired during 30 consecutive revolutions. Before each sequence, the turntable was rotated so that the rotor blade of interest was entering the fields of view of both cameras. The same turntable position was maintained until the rotor blades were leaving the fields of view—usually after about four or five azimuths ($\Delta\psi$ = 22.5–30°). Then the turntable was re-positioned and the process was repeated. Blade displacement measurements were limited to azimuths 90°± 30° and 270°± 30° because at other azimuths the fuselage of the test article blocked the view of one or the other camera.

Elastic bending and twist of the rotor blades were computed by comparing wind-on and reference (wind-off) coordinates of all targets in the rotor blade coordinate system. Photogrammetry yielded the object-space coordinates of the targets in tunnel coordinates; VSTARS provided reference coordinates in blade coordinates. The crux of the blade-displacement problem is to find the transformation, consisting of three unknown displacements and three unknown rotations, between these coordinate systems. This was accomplished by comparing the space coordinates of the targets designated as "fixed" or rigid (Figs. 3 and 6) at wind-on and reference conditions and finding the set of displacements and rotations that minimized differences between them. This is a nonlinear least-squares problem that was solved by the Levenberg-Marquardt algorithm [12]. The resulting transformation was applied to all targets, bringing them all into the rotor blade coordinate system. The remaining differences were due to elastic bending and twist.

The procedure just described addresses the same problem as model deformation measurement (MDM) of fixed wing vehicles. MDM, however, typically yields rotations pitch, yaw, and roll, whereas the rigid-body rotations most relevant to rotorcraft are pitch (about the blade feathering axis, x), flap (in the vertical x-z plane about the flapping hinge), and lead-lag (in the horizontal x-y plane about the lead-lag hinge). Therefore, the least-squares problem was solved in terms of the rotor angles directly. This required including two additional rotations (both known from the tunnel data system): rotor shaft angle-of-attack (α); and blade azimuth (ψ).

The instantaneous elastic bending and twist were computed from each pair of images from the two cameras. At each radial station (r / R) the out-of-plane bending (Δz) at the elastic axis (x/c = 0.25) was found by linear interpolation between Δz measurements at the leading- and trailing-edge targets at that station. The instantaneous elastic twist at each radial station was computed from: $\Delta twist = \tan^{-1}((\Delta z_{le} - \Delta z_{te})/(x_{te} - x_{le}))$. Note that the elastic twist is zero when the elastic out-of-plane displacements at the leading and trailing edges are the same. Average and standard deviations of the instantaneous measurements over the 30 revolutions were computed at each test point.

The images were analyzed using an in-house Windows-based application that draws on many sources including "The Photogrammetry Toolbox" developed by Liu and Burner [13].

V. Results

All of the tests were conducted at rotor RPM = 1090 and at a rotor shaft angle of attack (α) of -3°. At this RPM the rotor tip speed was 637 ft/sec. Thrust coefficient normalized by solidity (C_T / σ) was varied between 0.04 and 0.115. Free-stream velocity (V_∞) was set for advance ratios (μ) between 0.15 (V_∞= 96 ft/sec) and 0.39 (V_∞= 248 ft/sec). Test points were chosen to accommodate the thermography measurements.

Figure 6 shows typical images from both cameras. The grey scale has been adjusted to show as much detail as possible in the very dark images. The "fixed" targets used to compute the rigid-body transformation are indicated. Also visible are the targets on the ceiling that were used to compute the camera external orientations.

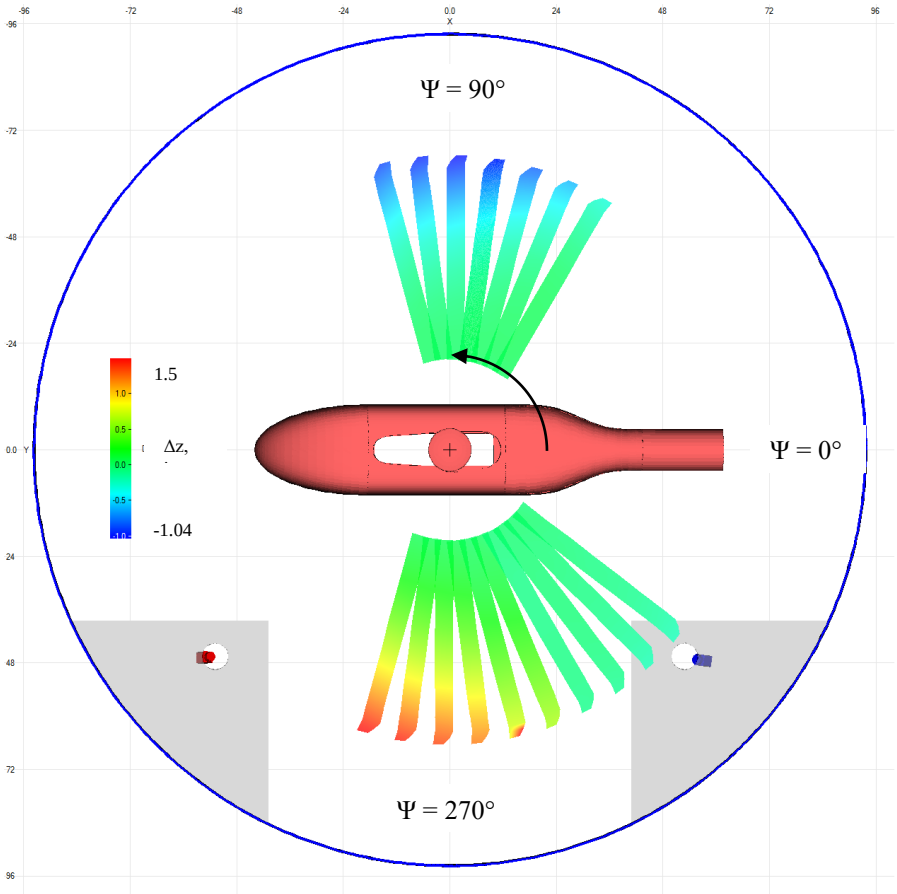

Fig. 8 Top view showing typical elastic bending over range of blade azimuth angles (C_T / σ = 0.1, μ = 0.3).

Results will be shown for measured elastic bending and twist as functions of radial station over the range of test conditions and azimuths at which the blade was visible to both cameras. Elastic bending and twist of each of the three blades are compared with each other. All of the bending data are at the elastic axis (quarter chord). Photogrammetry measurements of rigid-body displacements (pitch, flap and lag) are compared to measurements from the rotor data system. The sensitivities of both the elastic and rigid-body quantities to the choice of rigid-body targets are also examined.

A. Elastic deformations

Figure 8 is a top view of the test configuration that shows the test article and the range of blade azimuths were blade displacement measurements were made. At each azimuth a color overlay indicates the elastic bending for the test condition $C_T/\sigma = 0.1$ and $\mu = 0.3$. The blade tip bends up when the blade is retreating (ψ near 270°) and bends down when the blade is advancing (ψ near 90°). At this test condition both C_T/σ and μ were near their highest values.

1. Effect of azimuth (C_T/σ and μ constant)

Figure 9 presents plots of elastic bending along the elastic axis and twist of blade 1 versus radius at the same test condition as Fig. 8 (C_T / σ = 0.1; μ = 0.3) with blade azimuth as a parameter. Each data point is the average of 30 consecutive instantaneous measurements acquired over a time interval of 1.65 seconds. Error bars, mostly smaller than the symbols, indicate the standard deviations of the measurements. The tip of the advancing blade bends down as azimuth increases, reaching a maximum downward displacement of about 1 inch near ψ = 90°. The downward displacement diminishes as azimuth increases further. At each azimuth of the advancing blade the elastic twist varies smoothly from root to tip except at the span stations closest to the root and tip, where the blade planform changes abruptly. The advancing blade experiences a nose-down elastic twist that increases as azimuth increases. The measurements appear to resolve differences in elastic twist smaller than 0.1°. The tip of the retreating blade is already at its maximum observed upward displacement (about 1.5 in) before reaching ψ = 270°, and the upward displacement

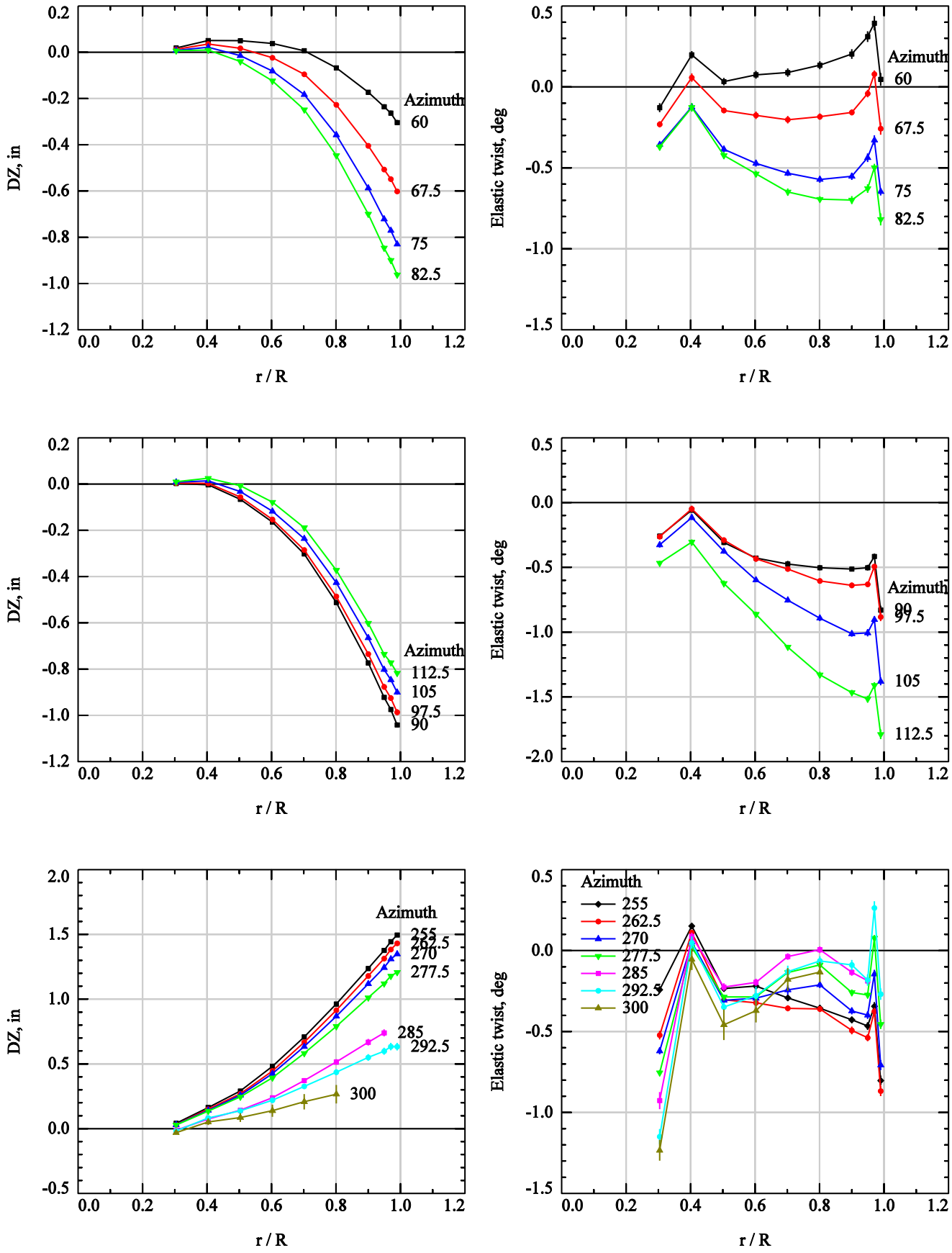

Fig. 9 Elastic bending (left) and twist (right) of advancing (top and middle) and retreating (bottom) blade ($C_T / \sigma = 0.1$, $\mu = 0.3$, blade 1).

decreases as azimuth increases. The variation of elastic twist of the blade is not as smooth when it is retreating compared to when it is advancing and the apparent discontinuities near the hub and tip are larger.

2. Effect of Thrust Coefficient (ψ and μ constant)

Figure 10 shows how changes in C_T/σ affected elastic bending and twist of blade 3 when it was advancing (ψ = 90°) and retreating (ψ = 270°) at a high advance ratio (μ = 0.3). When the blade was advancing, its tip was bent downward about 0.5 in, and increases in C_T/σ had very little effect on the bending. In contrast, when the blade was retreating, the upward displacement of the tip increased significantly with increasing C_T/σ. In addition, the standard deviations of the measurements at the higher thrusts were larger than at low thrust, indicating larger cycle-to-cycle bending variations. The measurements of elastic twist did not vary smoothly from hub to tip, and the effects of C_T/σ appear to be small at both ψ = 90° and ψ = 270°. The variations of elastic twist with radius, though not smooth, were very similar at all thrusts.

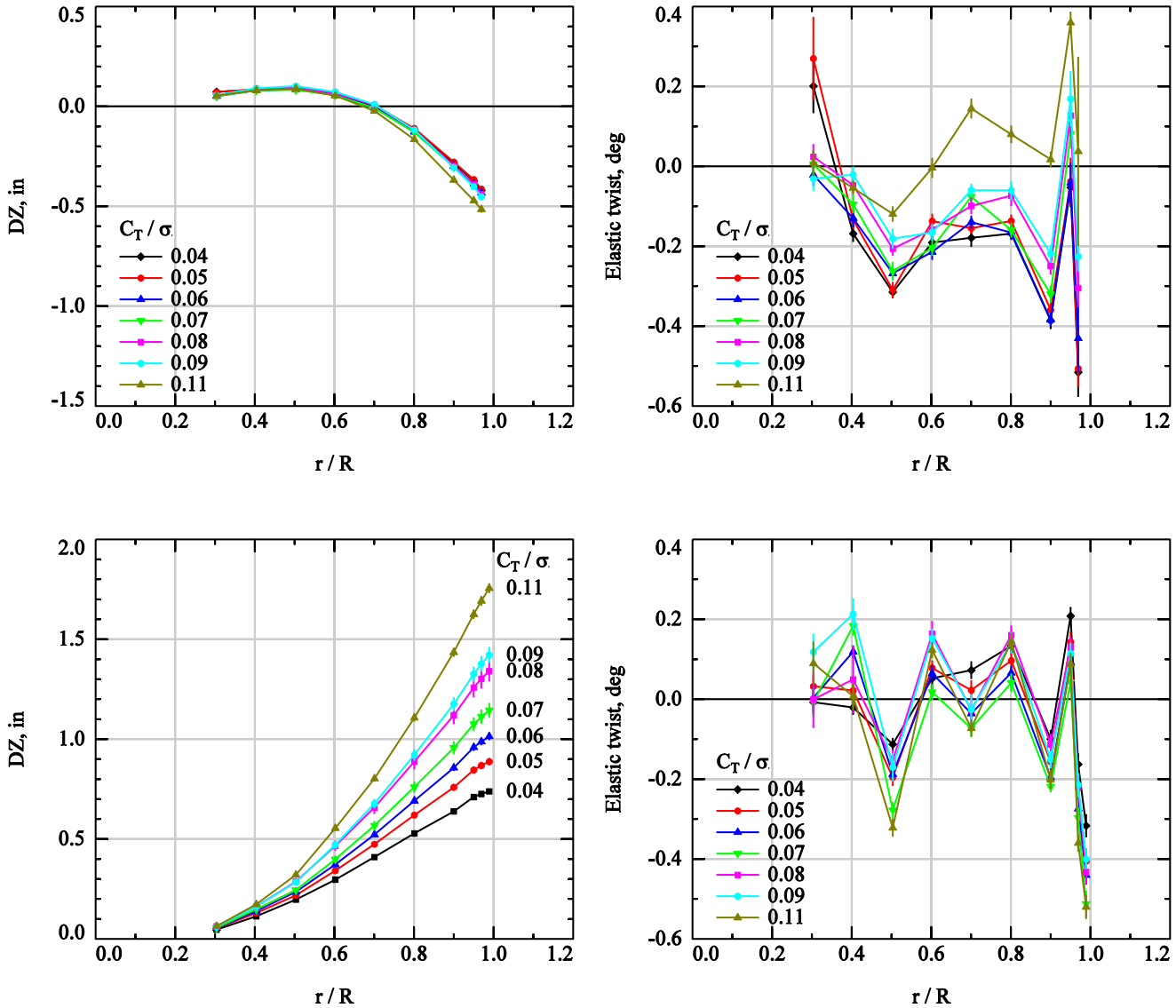

Fig. 10 Effect of C_T/σ on elastic bending (left) and twist (right) of advancing (ψ = 90°, top) and retreating (ψ = 270°, bottom) blade (μ = 0.3, blade 3).

3. Effect of Advance Ratio (ψ and C_T/σ constant)

The effects of increasing advance ratio on elastic bending and twist are shown in Figure 11 for a high thrust coefficient ($C_T/\sigma = 0.1$). The downward displacement of the advancing blade increased with increasing μ whereas the upward displacement of the retreating blade was largely unaffected. Elastic twist was small and negative at all three advance ratios at both $\psi = 90°$ and $\psi = 270°$, but there was no simple progression with μ.

4. Blade comparisons

In Figure 12, the elastic bending and twist of all three blades are compared at $\psi = 90°$ and $\psi = 270°$. The test conditions were the same for all three blades at each azimuth but conditions at the two azimuths were slightly different from each other. There were significant blade-to-blade differences in both bending and elastic twist both when the blades were advancing and retreating.

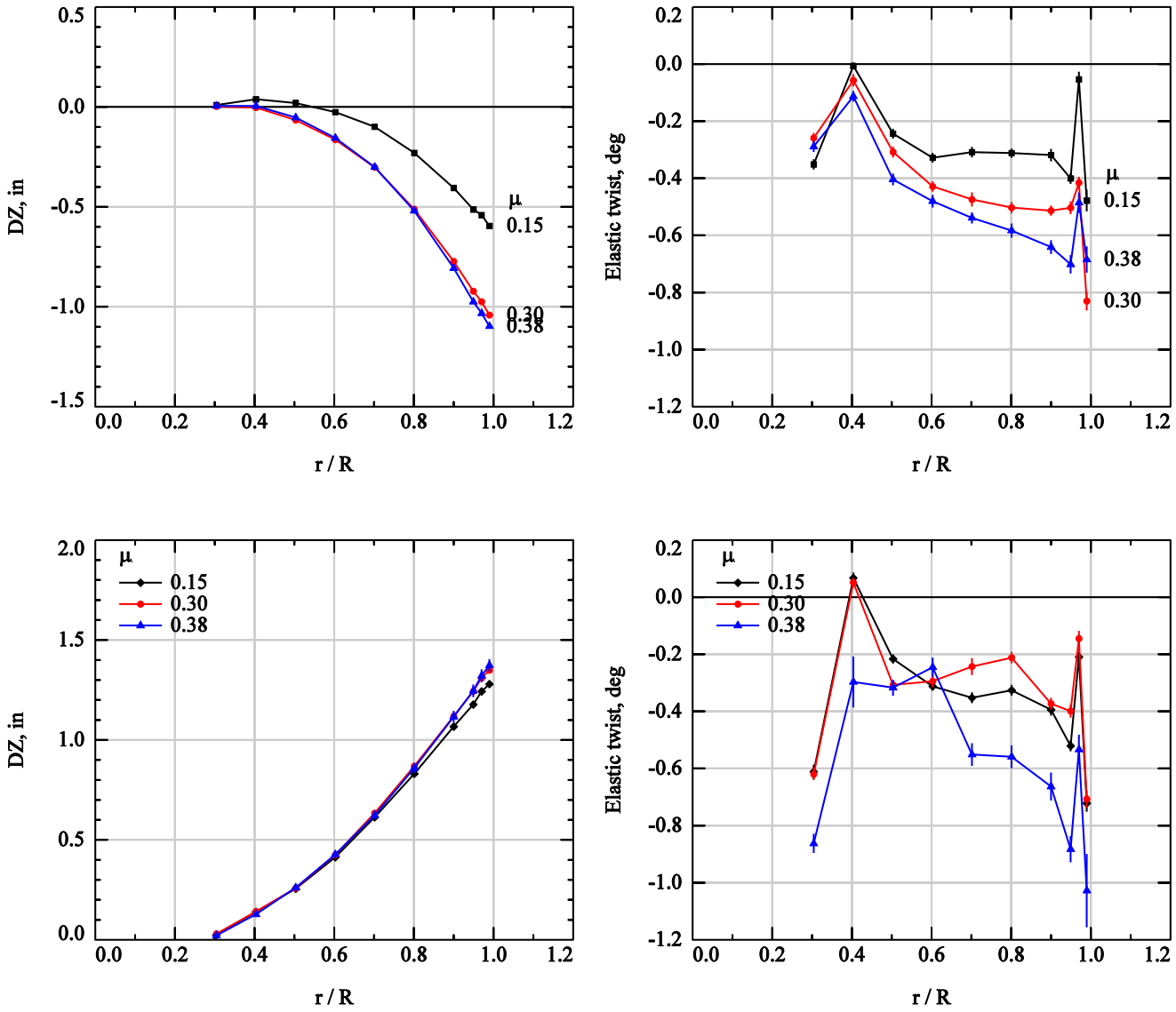

Fig. 11. Effect of μ on elastic bending (left) and twist (right) of advancing ($\psi = 90°$, top) and retreating ($\psi = 270°$, bottom) blade ($C_T / \sigma = 0.1$, blade 1).

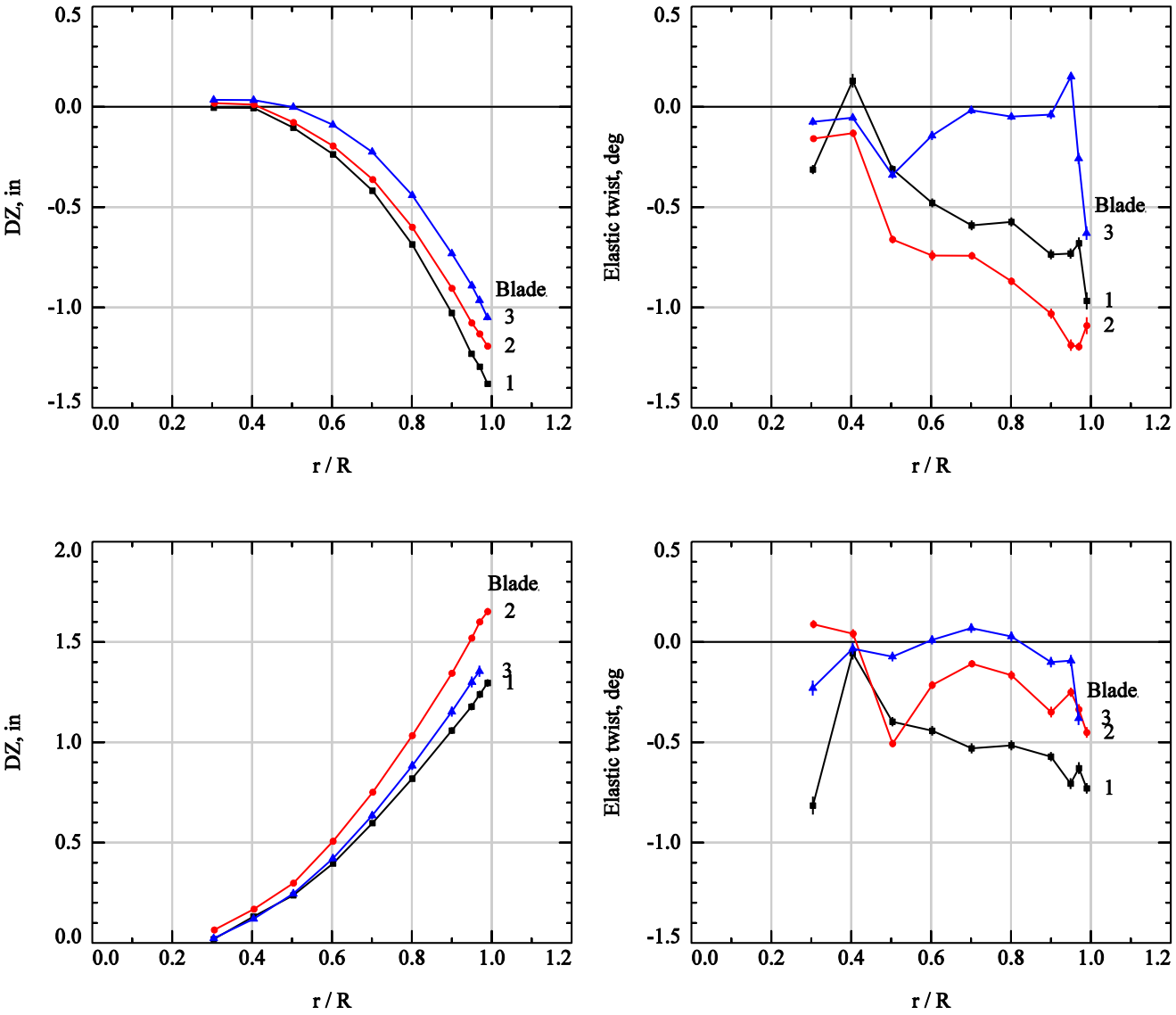

Fig. 12 Elastic bending (left) and twist (right) of blades 1-3: advancing (top, ψ = 90°, C_T / σ = 0.09, μ = 0.39) and retreating (bottom, ψ = 270°, C_T / σ = 0.1, μ = 0.3) blade.

5. Repeatability

Figure 13 compares elastic bending and twist measurements for test points repeated at the same test conditions and turntable positions. The bending measurements repeated within less than 0.1 in on both the advancing (ψ = 90°) and retreating (ψ = 270°) sides. Differences in elastic twist between repeated test points were large as 0.3°. Measurements that were repeated at the same test conditions but with the turntable (i.e., cameras) at different positions are shown in Fig. 14. The data repeat as well as repeated measurements at the same turntable position (Fig. 13), which suggests that bias errors due to differences in camera poses were small.

B. Rigid-body rotations (Pitch, flap, and lag)

The rotor data system provided independent measurements of pitch, flap, and lag angles at all test conditions for the full range of azimuths angles between 0 and 360°. These data were averaged over 256 consecutive revolutions of the rotor. Photogrammetry provided measurements over the restricted azimuths shown in Fig. 8, and the measurements were averaged over 30 consecutive revolutions. Figure 15 compares rotor data system (continuous line) and

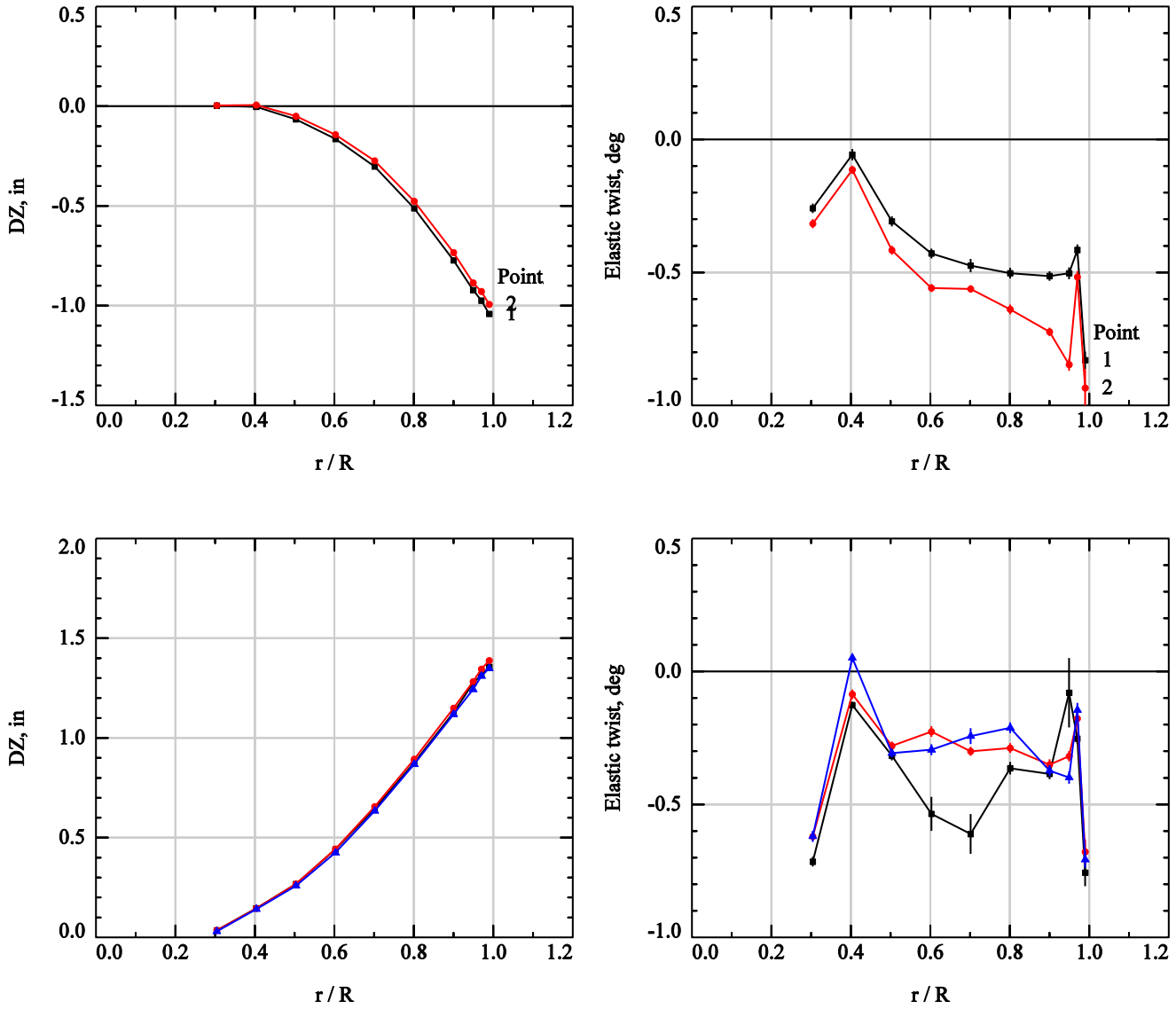

Fig. 13 Repeatability of elastic bending (left) and twist (right) measurements (same turntable positions): advancing (top, ψ = 90°) and retreating (bottom ψ = 270°); C_T / σ = 0.1, μ = 0.3, blade 1.

photogrammetry measurements (symbols) of pitch, flap, and lag angles of blade 3 at high and low C_T/σ (μ = 0.30). The photogrammetry measurements of pitch show the same trends with azimuth and C_T/σ as the rotor data system, but they are uniformly lower by about one degree. The photogrammetry flap measurements also agree with the rotor data system to within about one degree, but they are higher; and the lag angles measured by photogrammetry exceed those of the rotor data system by about two degrees.

Figure 16 plots the phase-averaged pitch, flap, and lag angles measured by the rotor data system ("EnsAve") versus the same angles measured by photogrammetry for all test points. Measurements for the three blades are color coded. There were only two test points (green) where photogrammetry measured blade 2. For perfect agreement the data would collapse to a straight line passing through the origin with slope 1. The photogrammetry and rotor-data-system measurements of pitch measurements show a uniform offset of about one degree for all three blades. The flap measurements show similar scatter although the more expanded scale makes it appear larger. The lag measurements for blades 2 (green) and 3 (red) are similar to each other, but quite different from blade 1 (black). The reason for the different offsets is illuminated by Figure 17, which compares photogrammetry and rotor-system lag measurements for

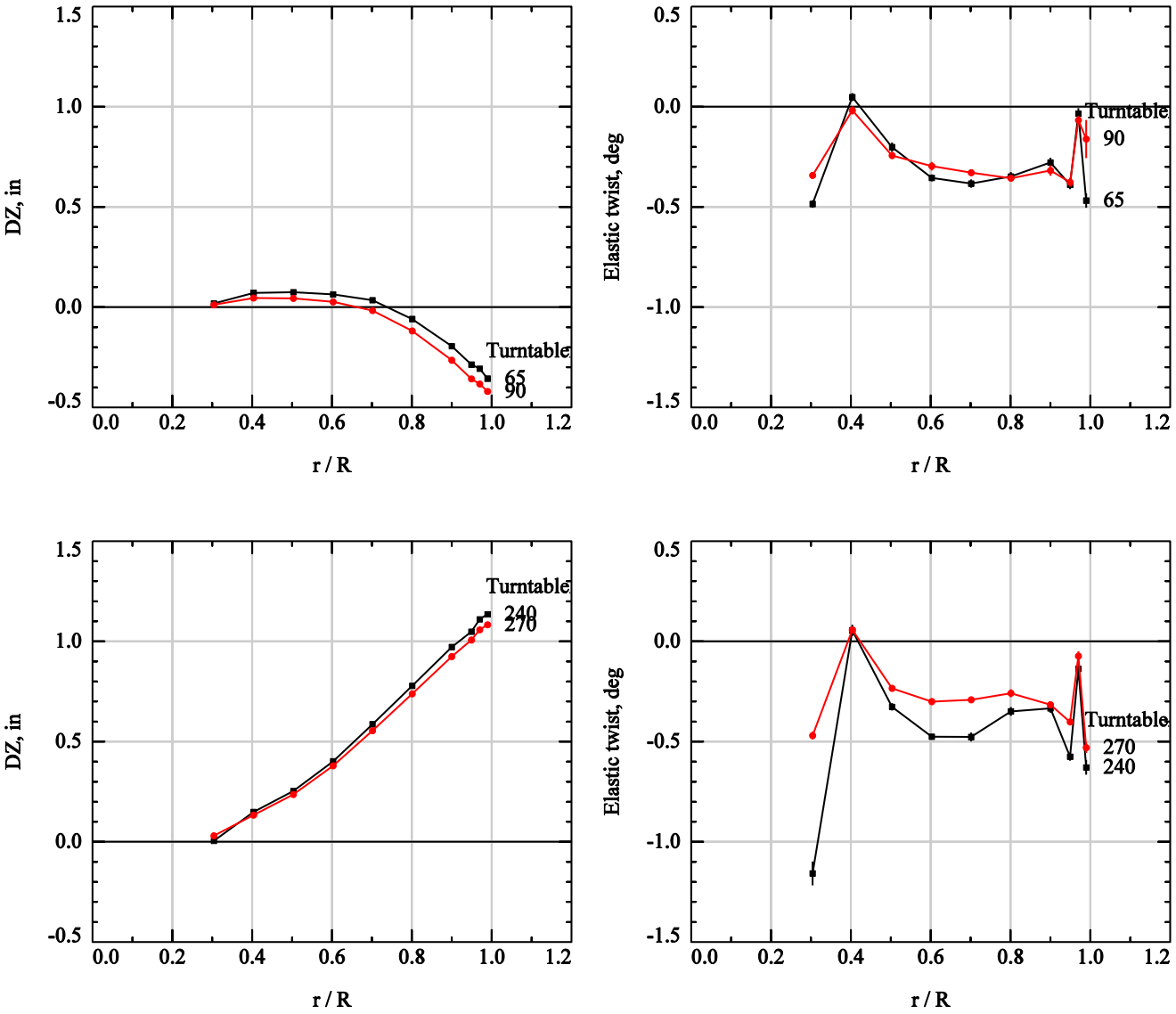

Fig. 14 Effect of different turntable positions on repeatability of elastic bending (left) and twist (right) measurements: advancing (top, ψ = 82.5°), and retreating (bottom, ψ = 262.5°); Ct / σ = 0.10, μ = 0.15) blade 1.

all three blades at the two test conditions where photogrammetry measured all three blades ($C_T/\sigma = 0.09$, $\mu = 0.39$ and $C_T/\sigma = 0.10$, $\mu = 0.30$). The photogrammetry lag measurements were nearly the same (within 0.5°) for all three blades whereas the rotor-system measurements show significantly different offsets at all azimuths for blades 2 and 3 compared to blade 1. This suggests bias errors in the rotor-system lag data that are different for each blade.

VI. Discussion

A. Uncertainties

There are many sources of uncertainty in photogrammetry measurements. Each instantaneous measurement is an approximate solution of an over-defined linear least-squares problem (for two cameras and three unknowns) and thus includes an error. The error depends on: how accurately the camera calibrations represent the transformation from object space to the image plane of each camera; how accurately points of interest (targets) can be located in the images; and the angle between the optical axes of the cameras (parallax). For blade-displacement and model deformation

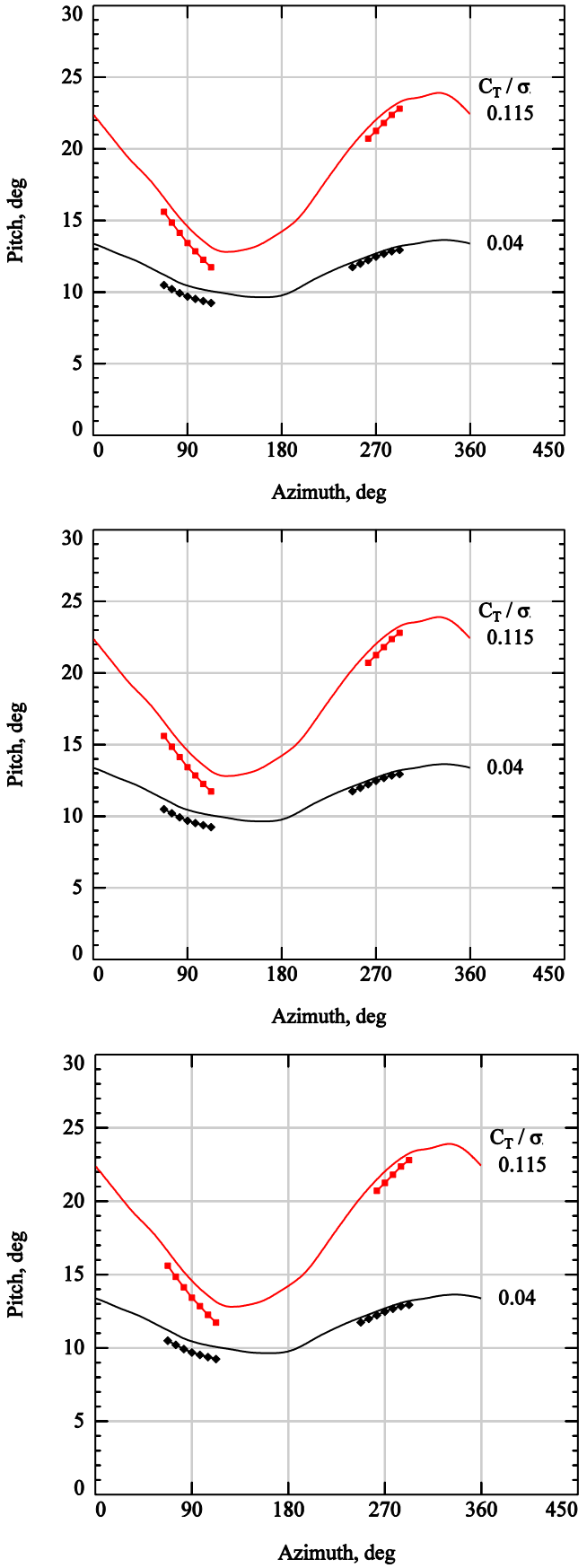

Fig. 15 Effect of C_T / σ on rigid-body pitch(top), flap (center), and lag (bottom)($\mu = 0.15$, blade 3).

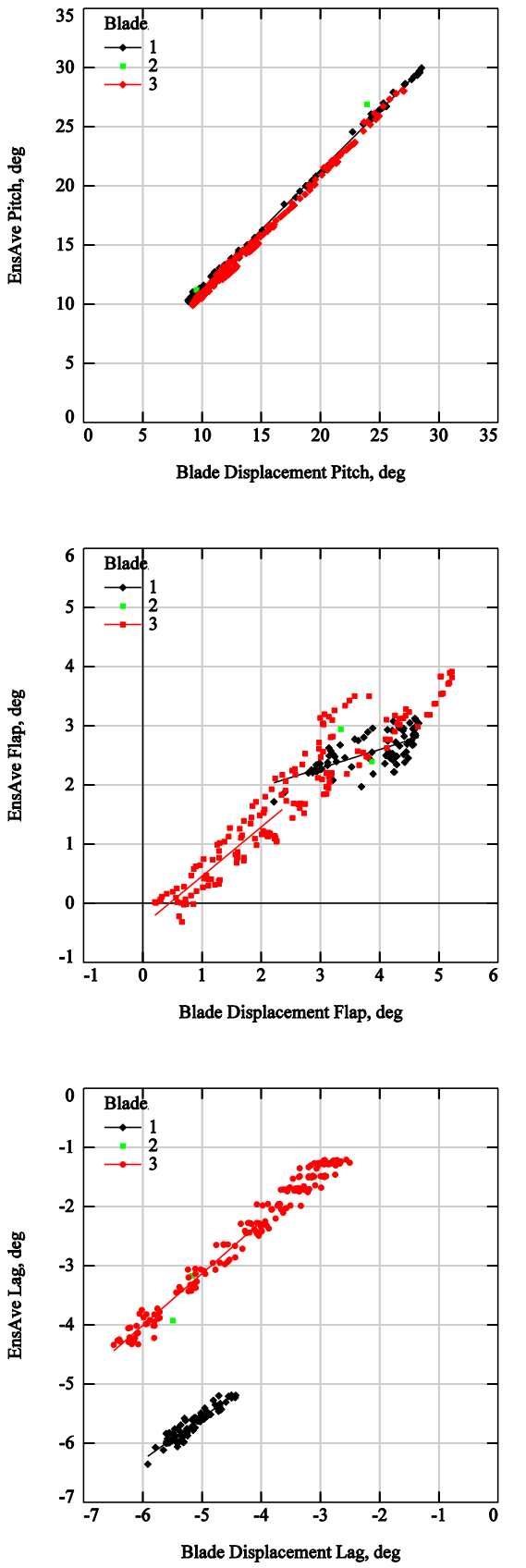

Fig. 16 Pitch (top), flap (center), and lag (bottom): rotor data system vs photogrammetry (all points).

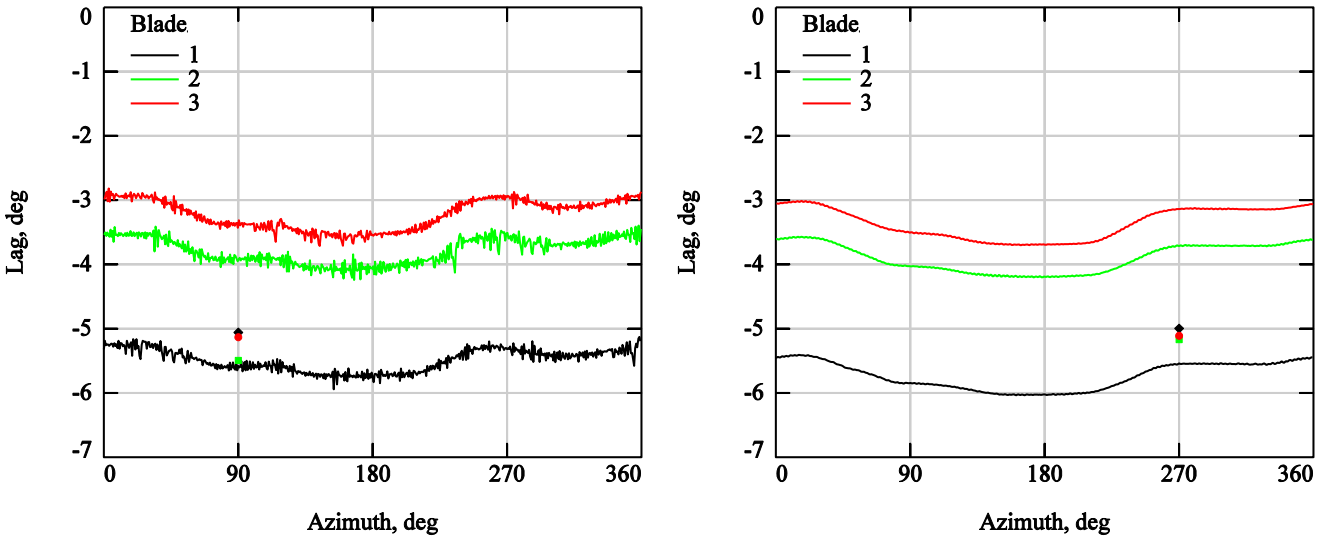

Fig. 17 Lag vs azimuth showing rotor data system (lines) and photogrammetry (symbols) data at the only two test points where photogrammetry measured all three blades: $C_T / \sigma = 0.09$, $\mu = 0.39$ (left); $C_T / \sigma = 0.10$, $\mu = 0.30$ (right).

measurements, there is the additional uncertainty of separating observed target displacements into contributions due to rigid-body motion and elastic deformation.

1. Target-finding uncertainties

The precision of the blade displacement measurements depended on how accurately and repeatably targets on the rotor blades could be located in the images from both cameras. Test cases using synthetic images of ideal pixelated targets showed that the target-finding algorithm could locate targets with an uncertainty of about 0.1 pixels. An error propagation analysis showed that a 0.1 pixel error in locating targets produced changes at the rotor tip of $\Delta z = 0.04$ in and Δtwist = 0.05°. These changes are linearly proportional to the target-finding uncertainty. Another indicator of random error is the standard deviation of measurements over 30 sequences at each test point. At the rotor tip these were typically $\sigma_z = 0.02$ in, $\sigma_{twist} = 0.09°$. These are high estimates because they include the effects of unsteadiness, not just target-finding uncertainty.

Each photogrammetry measurement includes a "re-projection" error, which, for each camera, is the difference between the measured pixel coordinates of the target and the pixel coordinates computed from the computed space coordinates of the target and the camera calibration. In the present test, the root-mean-squared of the re-projection errors at all targets at each test point was typically 1-2 pixels.

2. Camera vibration

Tunnel vibration inevitably leads to vibration of the cameras, resulting in small changes in the camera positions and point angles (pose) and, less likely, the focal length and principal point (internal orientation). The effects of vibration were evident as small (1-2 pixels) image-to-image changes in the positions of the targets on the ceiling that were used to compute the camera poses. The effects of these changes on the average blade displacement measurements were assessed for a typical 30-image test point by using the perturbed ceiling-target positions in each image to re-computed the pose of each camera at each instance. This procedure resulted in average bending and twist measurements that were nearly identical to those that were computed using the same poses for all images in the sequence. Thus, we conclude that the effects of tunnel vibration on the blade-displacement measurements were very small.

3. Bending of rigid-body targets

Accounting for rigid-body displacements and rotations was an important source of uncertainty in the elastic blade-displacement measurements. This was problematic because the "rigid-body" targets on the inboard portions of the blades were, in truth, elastically and not rigidly connected. This problem was aggravated by the placement of rigid-body targets on the fairing covering the notch at the blade root (see Fig. 3). In addition, the rigid-body targets were

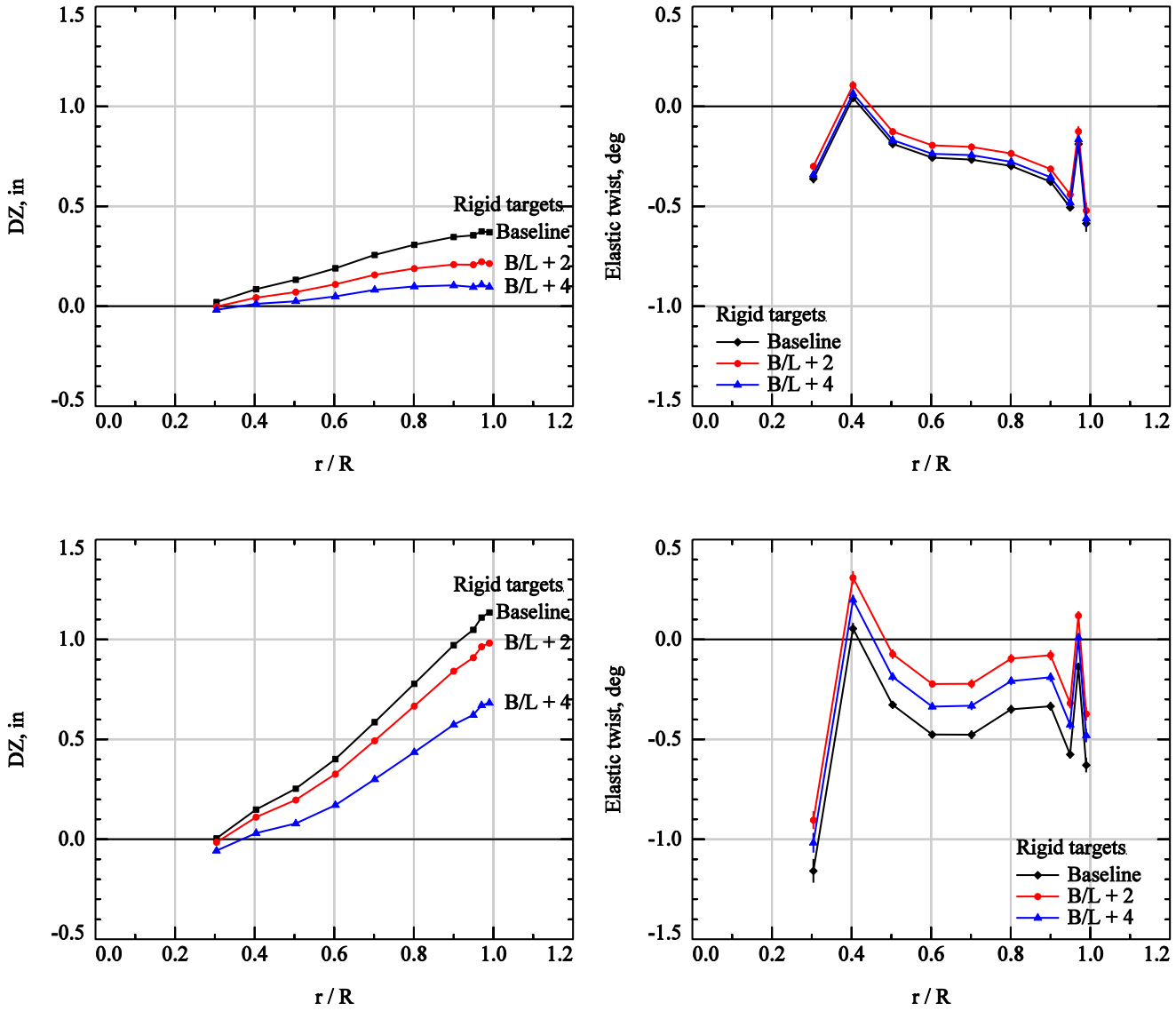

Fig. 18 Effect of rigid-body target set on elastic bending (left) and twist (right) measurements: advancing (top, ψ = 60°) and retreating (bottom, ψ = 262.5°); $C_T / \sigma = 0.10$, μ = 0.15, blade 1.

necessarily close together, and thus "close coupled." The effects of this close coupling was most severe at the rotor tip where errors in the rigid-body transformation were amplified by the long moment arm between the rigid-body targets and the tip. The sensitivity of the blade displacement measurements to the choice of rigid-body targets was observed by comparing, for a typical case, blade displacements computed using the baseline set of rigid-body targets to solutions computed using the baseline augmented by first two (r / R = 0.3) and then four (r / R = 0.4) flexible targets (Fig. 3). Including more outboard targets as rigid had very little effect on the downward displacement of the advancing blade but significantly reduced the measured upward displacement of the retreating blade (Fig. 18). This was likely due to the higher inboard loading on the retreating blade side resulting in higher deformation of the "rigid" targets. The effects on the elastic twist distribution were small (< 0.1°) for both the advancing and retreating blade. Augmenting the rigid-body target set had a small effect (< 0.5°) on pitch, flap, and lag measurements.

We note that in the UH-60 Airloads test, blade displacement measurements were corrected for bending of the inboard portion of the blade where rigid-body targets were located (r / R ≤ 0.35) by enforcing zero bending and elastic

twist at the hinge as well as setting radial derivatives of bending and elastic twist to zero [4]. These corrections have not been applied to the measurements presented here.

4. Elastic twist

Many of the elastic twist measurements varied smoothly with r / R over most of the blade radius. But in almost all cases, including the smoothest, there were large, abrupt changes in twist at stations near the root and at the swept tip. Elastic twist measurements tended to be smoother when the blade was advancing (Fig 9, top and center, right) than when it was retreating (Fig. 9, bottom-right). Indeed, many measured twist distributions on the retreating blade were not smooth anywhere on the blade. It should be noted, however, that the jaggedness of these twist distributions remained largely unchanged as azimuth or test parameters were varied (e.g., Fig. 10). Likewise, the apparent twist anomalies near the root and tip of the smoothest distributions persisted during parametric sweeps (Figs 9 and 11). Finally, blades 1 and 3 each had a different characteristic jagged distribution of Δtwist vs r / R (there were too few measurements of blade 2 to generalize). This phenomenon is not understood and is still under investigation. It may be due to a bias error; or it may reflect structural characteristics of the blades. One possible source of a structural uncertainty is a chord-wise row of dynamic pressures sensors located just outboard of the sweep break.

Each elastic twist measurement in the present test was computed from the ratio of two differences based on measurements at only two targets: $\Delta twist = \tan^{-1}((\Delta z_{le} - \Delta z_{te})/(x_{te} - x_{le}))$. It is likely that greater precision can be achieved in future tests by including more chord-wise targets at each radial station. This would allow computing Δtwist from a linear best fit of Δz vs x using data at all points at the radial station. This approach has been used for MDM measurements of a truss-braced wing model. For the UH-60A Airloads test there were three targets at each radial station. The requirement for the upcoming hover test (HVAB) is to measure elastic twist to within 0.1°.

B. Validation

There were no independent measurements of elastic bending and twist to which the photogrammetric blade-displacements could be compared. Nor were there systematic measurements of the static blades at all azimuths such as those made during the UH-60A Airloads test [4]. The only relevant measurements available for comparison were the pitch, flap, and lag data from the rotor data system. As we have seen, the photogrammetry measurements agreed with these data to within about 1°-2°. A small error in the rotor shaft angle of attack introduces an error of equal magnitude in the pitch angle measured by photogrammetry. The rotor shaft angle was known very accurately (0.004°), so uncertainty in shaft angle cannot account for the differences between the blade-displacement and rotor-data-system pitch measurements. Likewise, a small error in azimuth shows up as an error of equal magnitude in the photogrammetric lag measurements. Here the uncertainty was larger—about 0.5°, so it may account for some of the difference between the blade-displacement and rotor-data-system lag measurements.

C. Looking back at UH-60A Airloads Test; Looking forward to NFAC Hover Test (HVAB)

The present test served as a stepping stone between the UH-60A Airloads Test [4] and the upcoming hover test (HVAB) in the NFAC 80- by 120-Ft Wind Tunnel. In both the present test and the Airloads test, blade displacement of a rotor in forward flight were measured by stereo photogrammetry over a range of azimuths using cameras mounted in the floor of the test section. The rotor in the Airloads test was much larger (R = 322 in, full scale) than that in the present test (R = 67 in), and measurements were made over the full 360° of azimuth. This required eight cameras fitted with fish-eye lenses. In the present test the range of azimuths was limited to about 90 ± 30° and 270 ± 30° and there were only two cameras. The smaller scale and more limited coverage allowed the use of lenses with longer focal lengths and less distortion. In addition, the cameras in the present test had more than three times the resolution (12.5 vs 4 Mpixels) as the Airloads cameras. Together, these factors allowed nearly eight times the resolution of the model in the present test compared to Airloads. A complication of the present test compared to the Airloads test was that the cameras were not fixed at one position—they rotated with the turntable. This required that their poses be recomputed at each turntable position. In both tests, camera poses were computed using targets on the ceiling whose positions had been measured by VSTARS. Finally, the data-reduction methodology used in both tests was very similar. Elastic twist measurements in the Airloads test were based on three targets at each radius whereas in the present test twist was computed from only two targets—the minimum required.

The rotor blade geometry in the upcoming hover test (HVAB) will be the same as the blades of the present test. However, the rotor will have four blades instead of three, and it will be 40 ft above the floor of the test section instead of only seven. Photogrammetry measurements will be made by the same two cameras mounted on the floor of the test section, and the angle between their optical axes will be the same. For hover, measurements are not required over a wide range of azimuths, so the cameras will be fixed. The greater distance to the rotor will be compensated for by using longer focal length lenses, so the spatial resolution of the rotor blades will be about the same as in the present

test. Thus uncertainties in the positions of targets in the hover test are expected to be about the same as in the present test. However, the uncertainty of elastic twist measurements can be reduced by increasing the number of targets at each radial station, allowing a least-squares linear fit of Δz versus x.

VII. Conclusions

The blade-displacement measurements described in this paper had two purposes: first, to document elastic bending and twist of the blades in support of thermography measurements; and, second, to demonstrate that photogrammetry can measure elastic bending and twist with sufficient accuracy to meet requirements for upcoming hover tests in the NFAC 80- by 120-Ft test section. This capability was questioned because blade twist measurements made by photogrammetry in the UH-60A Airloads test were too uncertain to be of much use to the CFD community. In many cases the present measurements clearly resolved differences in elastic twist smaller than the 0.1° (Fig. 9), which is the requirement for the hover test. But almost all measurements also included unexplained abrupt but repeatable changes in twist near the blade root and tip. Many measured elastic twist distributions did not vary smoothly anywhere on the blade, especially when the blade was retreating. But the radial twist variations were repeatable as test parameters were varied. The reasons for these behaviors are not well understood and are still under investigation.

Acknowledgments

This work was supported by the US Army CCDC AvMC, the NASA Revolutionary Vertical Lift Technology (RVLT) Project, managed by Susan Gorton, and by the Innovative Measurements/T^3 Program, managed by Tom Jones at Langley Research Center. The authors also acknowledge the excellent support provided by the staff of the 14- by 22-Ft Wind Tunnel.

References

[1] Kushner, L.K., Schairer, E.T., Heineck, J.T., and Bell, J., "Model Deformation and Optical Angle of Attack Measurement System in the NASA Unitary Plan Wind Tunnel," AIAA Paper 2017-1052 presented at AIAA SciTech Forum, Grapevine, TX, Jan. 9-13, 2017.

[2] Drain, B.A.., Kushner, K.K., Schairer, E.T., and Heineck, J.T., "Model Deformation Measurements of the Truss-Braced Wing Aircraft in the NASA Ames 11- by 11-Ft Transonic Wind," AIAA Paper 2017-1054 presented at AIAA SciTech Forum, Grapevine, TX, Jan. 9-13, 2017.

[3] Schairer, Edward T., Kushner, Laura K., Garbeff, Theodore, Heineck, James T., "Model Deformation Measurements of Sonic Boom Models in the NASA Ames 9- by 7-Ft Supersonic Wind Tunnel," AIAA Paper 2015-1913 presented at the 53rd AIAA Aerospace Sciences Meeting, Kissemee, FL, Jan. 2015.

[4] Abrego, A.I., Meyn, L., Burner, A.W., and Barrows, D.A., "Summary of Full-Scale Blade Displacement Measurements of the UH-60A Airloads Rotor," presented at the AHS Technical Meeting on Aeromechanics Design for Vertical Lift, San Francisco, Jan. 20-22, 2016.

[5] Heineck, J.T., Spooner, H., Overmeyer, A., Gardner, A., Weiss, A., and Raffel, M., "Transition Measurements of Upper and Lower Rotor Blade Surfaces in Forward Flight with Thermography," to be presented at AIAA Aviation, 2020.

[6] Overmeyer, A., Heineck, J.T., Wolf, C.C., "Unsteady Boundary Layer Transition Measurements on a Rotor in Forward Flight," American Helicopter Society 74th Annual Forum, May 14-18, 2018, Phoenix, AZ.

[7] Heineck, J.T., Overmeyer, A., Wolf, C.C., Raffel, M., "Boundary Layer Transition Visualization of a Helicopter Blade in Forward Flight using Thermography," 18th International Symposium on Flow Visualization, Zurich, Switzerland, June 26-29, 2018.

[8] URL: https://www.geodetic.co/v-stars/ [retrieved 15 Mar. 2018].

[9] Fleming, G.A., "RASP: Rotor Azimuth Synchronization Program User's Guide, Version 1.3," NASA Langley Research Center, Feb. 6, 2008.

[10] Zhang, Z., "Flexible Camera Calibration by Viewing a Plane from Unknown Orientations," presented at International Conference on Computer Vision, Corfu, Greece, Sept. 1999, pp.666-673.

[11] Finley, T.D. and Tcheng, P., "Model attitude measurements at NASA Langley Research Center," AIAA Paper 92-0763, presented at the 30th AIAA Aerospace Sciences Meetings, Jan 6-9, 1992.

[12] Press, W.H., Flannery, B.P., Teukolsky, S.A., and Vetterling, W.T., *Numerical recipes, The Art of Scientific Computing*, Cambridge University press, Cambridge, 1986, pp. 523-528.

[13] Liu, T., and Burner, A.W., "Photogrammetry Toolbox Reference Manual," NASA CR 2014-218518, NASA Langley Research Center, Hampton, VA, Sept. 2014.